

## Disentangling Intracycle Interferences in Photoelectron Momentum Distributions Using Orthogonal Two-Color Laser Fields

Xinhua Xie (谢新华),<sup>1</sup> Tian Wang,<sup>2</sup> ShaoGang Yu,<sup>3</sup> XuanYang Lai,<sup>3</sup> Stefan Roither,<sup>1</sup> Daniil Kartashov,<sup>1</sup> Andrius Baltuška,<sup>1</sup> XiaoJun Liu,<sup>3,\*</sup> André Staudte,<sup>2,†</sup> and Markus Kitzler<sup>1,‡</sup>

<sup>1</sup>Photonics Institute, Technische Universität Wien, 1040 Vienna, Austria

<sup>2</sup>Joint Laboratory for Attosecond Science of the National Research Council and the University of Ottawa, Ottawa, Ontario K1A 0R6, Canada

<sup>3</sup>State Key Laboratory of Magnetic Resonance and Atomic and Molecular Physics, Wuhan Institute of Physics and Mathematics, Chinese Academy of Sciences, Wuhan 430071, China

(Received 25 July 2017; revised manuscript received 13 October 2017; published 11 December 2017)

We use orthogonally polarized two-color (OTC) laser pulses to separate quantum paths in the multiphoton ionization of Ar atoms. Our OTC pulses consist of 400 and 800 nm light at a relative intensity ratio of 10:1. We find a hitherto unobserved interference in the photoelectron momentum distribution, which exhibits a strong dependence on the relative phase of the OTC pulse. Analysis of model calculations reveals that the interference is caused by quantum pathways from nonadjacent quarter cycles.

DOI: 10.1103/PhysRevLett.119.243201

The momentum distributions of photoelectrons emitted during the interaction of intense laser pulses with atoms and molecules contain a wealth of information about the structure and field-induced attosecond dynamics in the target. This information can often be extracted by analyzing them in terms of semiclassical electron trajectories [1]. Within this semiclassical framework, the measured distributions can be understood as interferences of electron wave packets that reach the detector on direct or recolliding trajectories, giving rise to intercycle and intracycle fringes [2,3], holographic structures [4,5], and diffraction patterns [6–10]. Here, we use tailored laser fields, specifically orthogonally polarized two-color (OTC) fields [11], to gain control over the creation of interference structures in photoelectron momentum distributions. This permits us to experimentally disentangle a novel class of interference fringes from the many other structures in the measured distributions.

Interferences based purely on diffracting recolliding trajectories have been shown to provide structural information about the molecule with femtosecond temporal resolution [9,10,12]. On the other hand, interference fringes in the photoelectron spectrum arising from both direct and recolliding trajectories can be inverted to yield valence electron dynamics with attosecond resolution [3,5]. Two types of direct trajectories need to be distinguished for such an inversion: those launched with a periodicity of exactly one laser cycle giving rise to intercycle fringes, also referred to as above-threshold ionization peaks [13,14], and trajectories that originate from a single laser cycle, leading to intracycle interference fringes [2,3,15]. The resulting modulation of the intercycle peaks by the intracycle fringes can be interpreted as the diffraction of the emitted wave packets on a temporal grating [2]. Thus far, only intracycle fringes that originate from electron wave

packets emitted during adjacent quarter cycles of the optical wave—a situation that has been called the temporal double slit—have been considered theoretically [2,16–18] and observed in experiments [3,15,19,20].

In our experiment, OTC fields [11,21,22] are used for the generation of a tailored temporal grating for wave packet emission, which allows us to create and observe for the first time intracycle interferences from nonadjacent quarter cycles. The key to this achievement is the generation of an OTC field where the weak streaking component has half the frequency of the strong ionizing field component. Depending on the phase delay between the two colors, the two-dimensional character of the OTC fields maps the subcycle wave packet emission times into different regions of the momentum space. This solves the notorious problem of disentangling the different types of interference structures from measured photoelectron momentum distributions and allows the clear observation of the intracycle fringes from nonadjacent quarter cycles.

Disentanglement of different quantum paths using the two-dimensional mapping provided by OTC fields has been considered before [20,23–26]. Previously employed OTC pulses were generated by temporally overlapping an intense 800 nm pulse with a perpendicularly polarized 400 nm pulse of approximately equal [23,27–29] or weaker [30,31] peak intensity. In contrast, we invert the intensity ratio between long and short wavelength and use an intensity ratio of approximately 10:1 for 400 and 800 nm, respectively. Whereas multiphoton ionization in OTC pulses with a half-frequency streaking field has been investigated theoretically [32], our work explores this concept for the first time in an experiment.

In the experiment, OTC pulses were generated by combining *s*-polarized, 45 fs, 800 nm laser pulses, with

$p$ -polarized, 45 fs, 400 nm pulses, in a collinear geometry at a repetition rate of 5 kHz, as described in Refs. [23,27]. The peak intensity in the isolated 800 and 400 nm pulses was estimated (uncertainty about 30%) as  $0.2 \times 10^{14}$  and  $2 \times 10^{14}$  W/cm<sup>2</sup>, respectively. We used cold target recoil ion momentum spectroscopy (COLTRIMS) [33] to record the three-dimensional photoelectron momentum distribution of the single ionization of argon. Our COLTRIMS setup was described in detail previously [3,23,27]. In short, electrons and ions created in the laser focus were guided by weak uniform electric (1.54 V/cm) and magnetic (15.3 G) fields onto two multihit position- and time-sensitive detectors.

We define the field of the OTC pulse as [23]

$$\mathbf{E}(t) = \hat{E}_x f_x(t) \cos(\omega t) \mathbf{e}_x + \hat{E}_z f_z(t) \cos(2\omega t + \varphi) \mathbf{e}_z \quad (1)$$

with  $\hat{E}_{x,z}$  and  $f_{x,z}$  the peak field strengths and pulse envelopes along the 800 and 400 nm directions, respectively,  $\omega$  the laser frequency of the 800 nm field, and  $\varphi$  the relative phase between the two colors. Figure 1 illustrates how the orthogonally superposed 800 nm field streaks the subcycle ionization in the 400 nm field. According to the simple man's model [34,35] the final electron momentum after the laser pulse is given by  $\mathbf{p} = -\mathbf{A}(t_i)$  with  $\mathbf{A}(t) = -\int_{-\infty}^t \mathbf{E}(t') dt'$  the laser field's vector potential and  $t_i$  the birth time of the electron (atomic units are used throughout, unless stated otherwise). Figure 1(a) depicts  $\mathbf{A}(t)$  for each wavelength separately and for the two important limiting cases  $\varphi = 1.5\pi$  and  $\pi$ . Figure 1(b) shows the corresponding

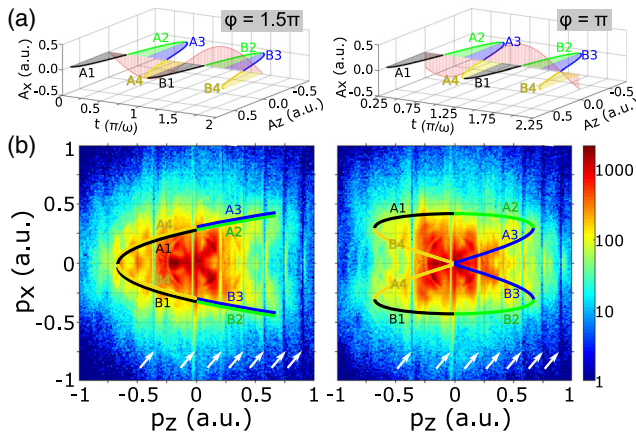


FIG. 1. (a) Vector potential of an OTC field for phase delays  $\varphi = 1.5\pi$  (left) and  $\varphi = \pi$  (right) over one optical cycle of the 800 nm field. The eight quarter cycles of the stronger 400 nm field are color coded and labeled by A1–A4 and B1–B4. The time window in each panel is adjusted to the reference quarter cycle A1. (b) Measured photoelectron momentum distributions of Ar ionized in a 45 fs OTC pulse, for the phase delays in (a). Superimposed on the momentum distributions is the simple man's prediction of the electron momentum,  $\mathbf{p} = -\mathbf{A}(t_i)$ , for  $\mathbf{A}(t)$  from panel (a). The arrows mark nodes (experimental artifacts) caused by the spectrometer magnetic field [33].

measured photoelectron momentum distributions in the polarization plane of the OTC pulse. On top of the photoelectron momentum distributions we superimposed  $\mathbf{p} = -\mathbf{A}(t_i)$  for  $t_i$  covering one optical cycle of the 800 nm field using the color code and labeling of Fig. 1(a).

In order to facilitate the analysis of the complex momentum distributions it is useful to transform the data into a polar coordinate system in the plane of polarization with the photoelectron energy  $E_{\text{kin}}$  as the radial coordinate. In Fig. 2(a) we have done this transformation for the data of Fig. 1(b). A polar angle of  $\theta = 0^\circ$  corresponds to a momentum towards the right side, i.e.,  $p_{z,400 \text{ nm}} > 0$  and  $p_{x,800 \text{ nm}} = 0$ . Apart from the sharp line features due to the experimental artifacts (marked by arrows), both spectra show pronounced structures and differ significantly at  $\theta = 180^\circ$ . Whereas for a phase of  $\varphi = \pi$  the photoelectron spectrum is only faintly structured, a rich interference carpet appears for a phase of  $\varphi = 1.5\pi$ . In the latter, a series of curved interference stripes is observed around  $\theta = 180^\circ$  and, moreover, a few pronounced peaks can be discerned within the stripes. The variation of these structures with the OTC field shape is visualized in the movie provided in the Supplemental Material [36].

To understand these interference structures, we turn to the strong-field approximation (SFA) theory. In the SFA theory, the transition amplitude of the photoelectron from the initial bound state  $|\psi_0\rangle$  to the final Volkov state  $|\psi_{\mathbf{p}}^V\rangle$  with the final momentum  $\mathbf{p}$  is given by [37,38]

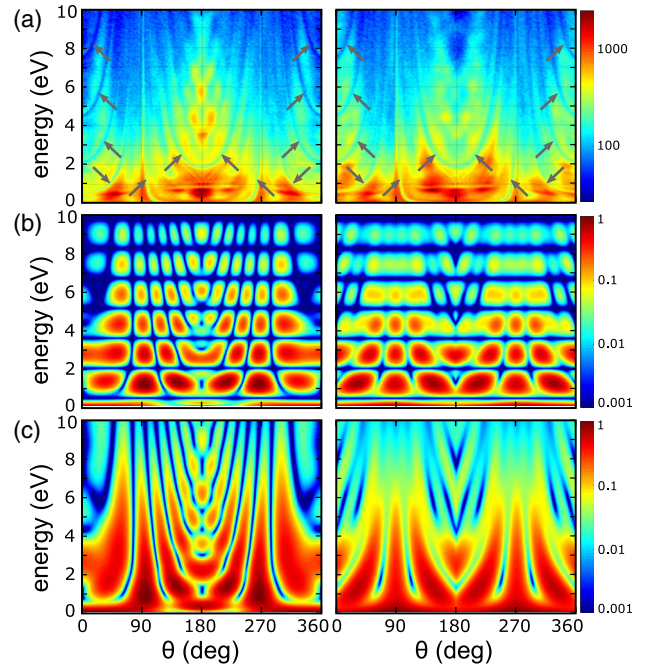


FIG. 2. Angle-resolved energy spectra of photoelectrons for a phase delay  $\varphi = 1.5\pi$  (left) and  $\varphi = \pi$  (right). (a) Experiment. (b) SFA calculation using Eq. (3). (c) SFA calculation with the OTC pulse restricted to one optical cycle of the 800 nm field. The arrows in (a) mark the experimental artifacts from Fig. 1(b).

$$M_{\mathbf{p}} = -i \int_{-\infty}^{\infty} dt (\mathbf{p} + \mathbf{A}(t)) \cdot \mathbf{r} \cdot \mathbf{E}(t) |\psi_0(r)\rangle e^{iS(\mathbf{p},t)}, \quad (2)$$

where  $\mathbf{r} \cdot \mathbf{E}(t)$  is the laser-field-electron interaction,  $S(\mathbf{p}, t) = -\frac{1}{2} \int_t^{\infty} dt' [\mathbf{p} + \mathbf{A}(t')]^2 + I_p t$  is the semiclassical action, and  $I_p$  denotes the ionization potential. For a sufficiently high intensity and low frequency of the laser pulse, the temporal integral in Eq. (2) can be evaluated with a high accuracy by the saddle-point method [39]. The corresponding transition amplitude then becomes

$$M_{\mathbf{p}} \sim \sum_s A_s(\mathbf{p}) e^{iS(\mathbf{p}, t_s)}, \quad (3)$$

where  $A_s(\mathbf{p}) = \sqrt{2\pi i / (\partial^2 S_{\mathbf{p}} / \partial t_s^2)} \langle \mathbf{p} + \mathbf{A}(t_s) | \mathbf{r} \cdot \mathbf{E}(t_s) | \psi_0(r) \rangle$ , and the index  $s$  runs over the relevant saddle points obtained by solving the saddle point equation  $[\mathbf{p} + \mathbf{A}(t)]^2 = -2I_p$ . Each saddle point corresponds to a quantum orbit. Physically, the transition amplitude  $M_{\mathbf{p}}$  represents the coherent superposition of all quantum orbits [39,40]. Equation (3) thus provides an intuitive formulation of interference patterns in photoelectron spectra.

In Fig. 2(b) we show the photoelectron spectrum  $d|M_{\mathbf{p}}|^2 / dE_{\text{kin}} d\theta$  calculated using Eq. (3) for the two phase delays  $\varphi = 1.5\pi$  and  $\pi$  with slightly lower laser peak intensities than in the experiment [ $0.15(1.5) \times 10^{14}$  W/cm<sup>2</sup> for 800 (400) nm] to achieve good agreement with the experimental data. This can be justified considering the experimental uncertainty. Our calculations reveal very distinct energy bands with a spacing of 1.55 eV, which are due to an intercycle interference that arises from the 800 nm component of the OTC field. Moreover, around  $\theta = 180^\circ$  the photoelectron distribution for  $\varphi = 1.5\pi$  features a much stronger ionization amplitude and more pronounced interference stripes than the distribution for  $\varphi = \pi$ . These features are in qualitative agreement with the experimental observations in Fig. 2(a).

In the following we will show that the distinct stripe structures around  $\theta = 180^\circ$  are caused by a nonadjacent intracycle interference, the focus of this Letter. The temporal grating created by the 800 nm component dominates the calculated energy spectrum. This discrepancy is due to the fact that the simulation in Fig. 2(b) assumes a cw OTC field, whereas the experiment has a pulse envelope with a full width at half maximum of intensity of 45 fs. In order to remove the cw effect in the simulation, we follow a procedure that was used previously for a linearly polarized two-color field [3] and restrict the ionization time of quantum orbits in Eq. (3) to one cycle of the 800 nm field for the remainder of the discussion. The resulting photoelectron spectrum is shown in Fig. 2(c). Thereby, a better agreement with the experimental data is achieved. In comparison to Fig. 2(b), it is clear that the intercycle interference features from the 800 nm field, i.e., the above-threshold ionization structures with an energy

spacing of 1.55 eV, disappear. On the other hand, the prominent stripes around  $180^\circ$ , as observed in the experiment, still persist. The remaining discrepancies between the experimental data and the SFA simulation in different angle and energy ranges can be ascribed to the influence of the parent ion's Coulomb potential, which is neglected in the present SFA theory but in OTC fields can have a significant influence, in particular on the relative electron yields emitted along different directions [18].

To understand the origin of the interference structures around  $180^\circ$  observed for  $\varphi = 1.5\pi$ , we investigate the separate contributions of the emission time windows A1–A4 and B1–B4, introduced in Fig. 1, to the overall photoelectron spectrum. The simple man's mapping of electron emission time to the asymptotic emission angle  $\theta$  in the polarization plane provided by the OTC field is shown in Fig. 3(a) for each quarter cycle of the 400 nm component. In agreement with this mapping, our SFA analysis shows that photoelectrons from the ionization time windows A2 and A3 will be mainly detected under angles  $0^\circ < \theta < 90^\circ$  [Fig. 3(c)], whereas photoelectrons emitted

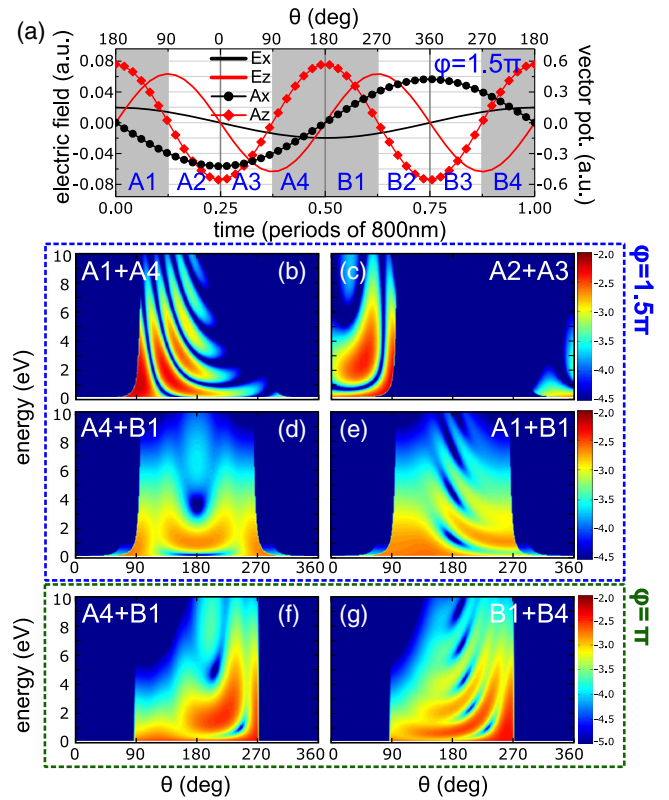


FIG. 3. (a) Electric fields ( $E_x, E_z$ ) and vector potentials ( $A_x, A_z$ ) for  $\varphi = 1.5\pi$  within one cycle of 800 nm. A1–A4 and B1–B4 denote the different ionization time windows introduced in Fig. 1. The top axis shows the asymptotic emission angle  $\theta$  of the photoelectron according to the simple man's model  $\mathbf{p} = -\mathbf{A}(t)$ . (b)–(g) SFA calculations for  $\varphi = 1.5\pi$  [(b)–(e)] and  $\varphi = \pi$  [(f),(g)] using Eq. (3) with quantum orbits from the different ionization time windows as indicated in the figures.

during  $A1$  and  $A4$  are observed as prominent stripes mainly within  $90^\circ < \theta < 180^\circ$  [Fig. 3(b)]. Because of their quantum widths, the wave packets extend beyond the classically expected ranges. Since the vector potential of the 800 nm field ( $x$  direction) has the opposite sign for the  $A$  and  $B$  quarter cycles [see Fig. 3(a)], the SFA momentum distributions of photoelectrons emitted during the corresponding  $B$  quarter cycles ( $B1 + B4$ ,  $B2 + B3$ ) are exact mirror images of Figs. 3(b) and 3(c) about the  $180^\circ$  axis and are, thus, not explicitly shown in Fig. 3.

Comparing Fig. 3(c) with the left panel of Fig. 2(c), it becomes clear that the interference patterns at  $0^\circ < \theta < 90^\circ$  are due to trajectories emitted from adjacent quarter cycles of the 400 nm field component ( $A2$  and  $A3$ ). This intracycle interference corresponds to the well-known temporal double slit and has been widely investigated in the literature [2,3,41,42]. In contrast, our analysis reveals that the stripes at  $90^\circ < \theta < 270^\circ$  visible for  $\varphi = 1.5\pi$  in Fig. 2(c) are from the interference of two kinds of orbits from nonadjacent quarters of the 400 nm field ( $A1 + A4$ ,  $B1 + B4$ ). This type of intracycle interference has not been observed or identified in experiment before, to the best of our knowledge. In fact, this intracycle interference of nonadjacent quarter cycle ionization also exists for a single-color field, see, e.g., Ref. [43]. However, in a single-color field, the two kinds of the intracycle interference structures appear in the same regions of the momentum space. Thus, the overlap of the two types of intracycle interferences obscures the nonadjacent intracycle interference. In contrast, the two-dimensional OTC field with a weaker half-frequency component drives the two orbits corresponding to the adjacent intracycle interference to different quarters of the photoelectron spectra, facilitating the detection of the nonadjacent intracycle interferences.

Our SFA simulations show that the interference stripes from this novel nonadjacent intracycle interference are much finer than those of the adjacent intracycle interference. The reason is that the ionization delays of the electron orbits for the nonadjacent intracycle interference are larger than those of the adjacent ones and, thus, the change of the corresponding action difference of the two orbits is more sensitive to the momentum of the photoelectron. This result is analogous to the double-slit interference [15], for which the stripe width on the screen is inversely proportional to the distance of the two slits. It is this novel intracycle interference, through which the fine and bent fringes at  $90^\circ < \theta < 270^\circ$  for  $\varphi = 1.5\pi$  are formed.

To further confirm this assessment, we plot in Figs. 3(d) and 3(e) other interference structures that can be observed in the range  $90^\circ < \theta < 270^\circ$  and might contribute to the overall momentum distribution. These structures, which are intracycle [Fig. 3(d)] and intercycle interferences [Fig. 3(e)] of the 400 nm field emitted during quarter cycles  $A4 + B1$  and  $A1 + B1$ , respectively, are broader and much weaker than the nonadjacent intracycle structures from  $A1 + A4$

and, thus, cannot account for the experimentally observed sharp features. The intercycle structures from  $A1 + B1$  somewhat contribute to the distinct peaks that are present on the background of these stripes around  $\theta = 180^\circ$  in both the measured [Fig. 2(a)] and total SFA [Fig. 2(c)] distributions. However, the dominant contributions to these peaks come from the coherent superposition of the nonadjacent intracycle interferences, i.e., a superposition of the  $A1 + A4$  structures from Fig. 3(b) with their mirrored counterparts from  $B1 + B4$ .

It is worth noting that the observation of the nonadjacent intracycle interference is strongly dependent on the phase delay of the OTC pulse [compare the left and right panels in Fig. 2(a) and also see the movie in the Supplemental Material [36]]. The reason is that by the variation of  $\varphi$  the OTC field shape changes, which results in completely different electron dynamics. To visualize this, we consider the OTC field with  $\varphi = \pi$  shown in the right panel of Fig. 1(a). We first discuss the nonadjacent intracycle interferences of the 400 nm field originating from the quarter cycles  $B1 + B4$ , shown in Fig. 3(g). As can be seen, the intensity of the interference pattern is significantly reduced as compared to the corresponding one for  $\varphi = 1.5\pi$  shown in Fig. 3(b). The reason is that for  $\varphi = \pi$  electrons from  $B1$  and  $B4$  are mainly observed in different quarters of the momentum plane, i.e.,  $180^\circ < \theta < 270^\circ$  for  $B1$  and  $90^\circ < \theta < 180^\circ$  for  $B4$  [cf. right panel of Fig. 1(a)]. In contrast, as the electron orbit from  $A4$  is classically allowed for  $180^\circ < \theta < 270^\circ$ , it can interfere with that from  $B1$  and, thus, the interference from the adjacent quarter cycles  $A4 + B1$  becomes much more prominent than that from the nonadjacent ones,  $B1 + B4$ . The interference from the adjacent quarter cycles  $A4 + B1$  [Fig. 3(f)], however, leads to much broader stripes and is also mainly observed at lower energy. As a result, no clear stripe structure related to the nonadjacent intracycle interference can be observed for  $\varphi = \pi$ , consistent with the experimental data in Fig. 2(a).

Concluding, we have demonstrated that the temporal grating in an OTC pulse can separate two classes of interfering intracycle quantum paths that evolve on two different time scales. In our experiment, the two-dimensional character of an OTC field with a weaker half-frequency component maps their contributions to different regions in momentum space facilitating their disentanglement. We envision that the coupling of subcycle time and space provided by OTC fields, as demonstrated by our experiment, can be exploited also for observing attosecond phenomena that lead to spatiotemporal variations of charge density. Careful analysis of intracycle interferences in OTC fields should thus permit the observation of subcycle variations of the ionization probability, caused, for example, by hole-wave packets after ionization [44]. This might be of particular interest for studying charge density oscillations in molecules that are properly oriented with respect to the spatiotemporal evolution of the OTC

field. We believe that photoelectron intracycle interferometry has a potential for resolving attosecond dynamics that is largely untapped. OTC pulses hold a key to unlock this potential.

We acknowledge funding by the Austrian Science Fund (FWF) under Grants No. P28475-N27, No. P25615-N27, No. P21463-N22, and No. SFB-F49 NEXTLite, by the National Basic Research Program of China (Grant No. 2013CB922201), and by the National Natural Science Foundation of China (Grants No. 11334009 and No. 11474321). Financial support from the National Science and Engineering Research Council, Discovery Grant No. 419092-2013-RGPIN, is gratefully acknowledged. T.W. acknowledges funding by the Chinese Scholarship Council.

\*xjliu@wipm.ac.cn

†andre.staudte@nrc-cnrc.gc.ca

\*markus.kitzler@tuwien.ac.at

- [1] D. B. Milošević, G. G. Paulus, D. Bauer, and W. Becker, *J. Phys. B* **39**, R203 (2006).
- [2] D. G. Arbó, K. L. Ishikawa, K. Schiessl, E. Persson, and J. Burgdörfer, *Phys. Rev. A* **81**, 021403 (2010).
- [3] X. Xie, S. Roither, D. Kartashov, E. Persson, D. Arbó, L. Zhang, S. Gräfe, M. Schöffler, J. Burgdörfer, A. Baltuška *et al.*, *Phys. Rev. Lett.* **108**, 193004 (2012).
- [4] Y. Huismans, A. Rouzée, A. Gijsbertsen, J. H. Jungmann, A. S. Smolkowska, P. S. W. M. Logman, F. Lépine, C. Cauchy, S. Zamith, T. Marchenko *et al.*, *Science* **331**, 61 (2011).
- [5] M. Haertelt, X.-B. Bian, M. Spanner, A. Staudte, and P. B. Corkum, *Phys. Rev. Lett.* **116**, 133001 (2016).
- [6] D. Ray, B. Ulrich, I. Bocharova, C. Maharjan, P. Ranitovic, B. Gramkow, M. Magrakvelidze, S. De, I. Litvinyuk, A. Le *et al.*, *Phys. Rev. Lett.* **100**, 143002 (2008).
- [7] M. Okunishi, T. Morishita, G. Prümper, K. Shimada, C. D. Lin, S. Watanabe, and K. Ueda, *Phys. Rev. Lett.* **100**, 143001 (2008).
- [8] M. Meckel, D. Comtois, D. Zeidler, A. Staudte, D. Pavicic, H. C. Bandulet, H. Pépin, J. C. Kieffer, R. Dörner, D. M. Villeneuve *et al.*, *Science* **320**, 1478 (2008).
- [9] C. I. Blaga, J. Xu, A. D. DiChiara, E. Sistrunk, K. Zhang, P. Agostini, T. a. Miller, L. F. DiMauro, and C. D. Lin, *Nature (London)* **483**, 194 (2012).
- [10] B. Wolter, M. G. Pullen, A.-T. Le, M. Baudisch, K. Doblhoff-Dier, A. Senftleben, M. Hemmer, C. D. Schroter, J. Ullrich, T. Pfeifer *et al.*, *Science* **354**, 308 (2016).
- [11] M. Kitzler and M. Lezius, *Phys. Rev. Lett.* **95**, 253001 (2005).
- [12] J. Xu, Z. Chen, A.-T. Le, and C. D. Lin, *Phys. Rev. A* **82**, 033403 (2010).
- [13] P. Agostini, F. Fabre, G. Mainfray, G. Petite, and N. K. Rahman, *Phys. Rev. Lett.* **42**, 1127 (1979).
- [14] R. R. Freeman and P. H. Bucksbaum, *J. Phys. B* **24**, 325 (1991).
- [15] F. Lindner, M. G. Schätzel, H. Walther, A. Baltuška, E. Goulielmakis, F. Krausz, D. B. Milošević, D. Bauer, W. Becker, and G. G. Paulus, *Phys. Rev. Lett.* **95**, 040401 (2005).
- [16] D. G. Arbó, E. Persson, and J. Burgdörfer, *Phys. Rev. A* **74**, 063407 (2006).
- [17] D. G. Arbó, K. L. Ishikawa, E. Persson, and J. Burgdörfer, *Nucl. Instrum. Methods Phys. Res., Sect. B* **279**, 24 (2012).
- [18] S. G. Yu, Y. L. Wang, X. Y. Lai, Y. Y. Huang, W. Quan, and X. J. Liu, *Phys. Rev. A* **94**, 033418 (2016).
- [19] R. Gopal, K. Simeonidis, R. Moshhammer, T. Ergler, M. Dürr, M. Kurka, K.-U. Kühnel, S. Tschuch, C.-D. Schröter, D. Bauer *et al.*, *Phys. Rev. Lett.* **103**, 053001 (2009).
- [20] M. Richter, M. Kunitski, M. Schöffler, T. Jahnke, L. P. H. Schmidt, M. Li, Y. Liu, and R. Dörner, *Phys. Rev. Lett.* **114**, 143001 (2015).
- [21] M. Kitzler, X. Xie, A. Scrinzi, and A. Baltuška, *Phys. Rev. A* **76**, 011801 (2007).
- [22] M. Kitzler, X. Xie, S. Roither, A. Scrinzi, and A. Baltuška, *New J. Phys.* **10**, 025029 (2008).
- [23] L. Zhang, X. Xie, S. Roither, D. V. Kartashov, Y. Wang, C. Wang, M. Schöffler, D. Shafir, P. B. Corkum, A. Baltuška *et al.*, *Phys. Rev. A* **90**, 061401 (2014).
- [24] X. Xie, *Phys. Rev. Lett.* **114**, 173003 (2015).
- [25] J.-W. Geng, W.-H. Xiong, X.-R. Xiao, L.-Y. Peng, and Q. Gong, *Phys. Rev. Lett.* **115**, 193001 (2015).
- [26] M. Richter, M. Kunitski, M. Schöffler, T. Jahnke, L. P. H. Schmidt, and R. Dörner, *Phys. Rev. A* **94**, 033416 (2016).
- [27] L. Zhang, X. Xie, S. Roither, Y. Zhou, P. Lu, D. V. Kartashov, M. Schöffler, D. Shafir, P. B. Corkum, A. Baltuška *et al.*, *Phys. Rev. Lett.* **112**, 193002 (2014).
- [28] X. Gong, C. Lin, F. He, Q. Song, K. Lin, Q. Ji, W. Zhang, J. Ma, P. Lu, Y. Liu *et al.*, *Phys. Rev. Lett.* **118**, 143203 (2017).
- [29] M. Han, P. Ge, Y. Shao, M. Liu, Y. Deng, C. Wu, Q. Gong, and Y. Liu, *Phys. Rev. Lett.* **119**, 073201 (2017).
- [30] Q. Song, P. Lu, X. Gong, Q. Ji, K. Lin, W. Zhang, J. Ma, H. Zeng, and J. Wu, *Phys. Rev. A* **95**, 013406 (2017).
- [31] X. Gong, P. He, Q. Song, Q. Ji, H. Pan, J. Ding, F. He, H. Zeng, and J. Wu, *Phys. Rev. Lett.* **113**, 203001 (2014).
- [32] M. Li, J.-W. Geng, M.-M. Liu, X. Zheng, L.-Y. Peng, Q. Gong, and Y. Liu, *Phys. Rev. A* **92**, 013416 (2015).
- [33] R. Dörner, V. Mergel, O. Jagutzki, L. Spielberger, J. Ullrich, R. Moshhammer, and H. Schmidt-Böcking, *Phys. Rep.* **330**, 95 (2000).
- [34] H. Van Linden van den Heuvell and H. Muller, Limiting cases of excess-photon ionization, in *Proceedings of the 4th Int. Conf. Multiphot. Process., JILA, Boulder, Colorado, 1987*, edited by S. J. Smith and P. L. Knight (Cambridge University Press, Cambridge, England, 1988), pp. 25–34.
- [35] P. B. Corkum, N. H. Burnett, and F. Brunel, *Phys. Rev. Lett.* **62**, 1259 (1989).
- [36] See Supplemental Material at <http://link.aps.org/supplemental/10.1103/PhysRevLett.119.243201> for a movie showing the variation of the interference structures in the measured photoelectron distributions with the relative phase between the two colors.
- [37] H. Reiss, *Phys. Rev. A* **22**, 1786 (1980).
- [38] D. B. Milošević and F. Ehlotzky, *Phys. Rev. A* **58**, 3124 (1998).

- [39] C. Figueira de Morisson Faria, H. Schomerus, and W. Becker, *Phys. Rev. A* **66**, 043413 (2002).
- [40] W. Becker, F. Grasbon, R. Kopold, D. B. Milošević, G. G. Paulus, and H. Walther, *Adv. At. Mol. Opt. Phys.* **48**, 35 (2002).
- [41] M. Li, X. Sun, X. Xie, Y. Shao, Y. Deng, C. Wu, Q. Gong, and Y. Liu, *Sci. Rep.* **5**, 8519 (2015).
- [42] X. Lai and C. Figueira de Morisson Faria, *Phys. Rev. A* **88**, 013406 (2013).
- [43] A. S. Maxwell, A. Al-Jawahiry, T. Das, and C. Figueira de Morisson Faria, *Phys. Rev. A* **96**, 023420 (2017).
- [44] Z.-h. Loh and S. R. Leone, *J. Phys. Chem. Lett.* **4**, 292 (2013).